

The CAD-Compatible VHP-Male Computational Phantom



Gregory M. Noetscher

1 Introduction

Computational human phantoms are an integral part of the design process in many areas of modern science and technology; this is especially true for computational electromagnetics (CEM). A review of available literature suggests that, since the very inception of CEM, its practitioners have used various model surrogates (primitive shapes, various combinations thereof, further refined models, etc.) to demonstrate the use of numerical modelling for the estimation of a body's response to external electromagnetic stimulation. The convergence of a number of disparate disciplines, including highly refined medical image collection techniques, advanced image processing, development of efficient simulation algorithms and supercomputing hardware, has resulted in computational human phantoms at a level of detail previously thought impossible.

Inspiration for the creation of the Visible Human Project (VHP)-Male model, presented herein, was the design and use of the VHP-Female model [15], which was constructed in the mid-2010s, adopted by the IEEE International Committee on Electromagnetic Safety for use as simulation of specific absorption rate (SAR), and used in a host of commercial and academic applications [2–4, 8, 12–14, 16, 17]. Throughout the development of the VHP-Female model, it became extremely apparent that compatibility with common computer-aided design (CAD) tools and interfaces was highly advantageous and enabled maximum use of the model in a variety of simulation methodologies, including the finite element method (FEM), boundary element method (BEM), finite-difference time-domain (FDTD) method and experimental methods, including the coupled boundary element-fast multipole

G. M. Noetscher (✉)

Electrical and Computer Engineering Department, Worcester Polytechnic Institute,
Worcester, MA, USA

e-mail: gregn@wpi.edu

© The Author(s) 2021

S. N. Makarov et al. (eds.), *Brain and Human Body Modeling 2020*,
https://doi.org/10.1007/978-3-030-45623-8_19

309

method (BEM-FMM) [10]. Due to the successful implementation of the female model and the demand for a male version, the steps described below were undertaken for its construction. It is our sincere hope that the model will be adapted in a manner similar to its predecessor.

This work is organized in the following manner. Section 2 (Materials and Methods) documents the model construction process, including a description of the source data and mesh processing techniques. Section 3 (Results and Discussion) depicts the outcomes of mesh construction, global model assembly and baseline simulation. Section 4 (Conclusions) provides a summary of the work, together with plans for future work, suggestions for augmentations to the model and potential applications for which this model may be suitable.

2 Materials and Methods

2.1 Source Data

As its name would suggest, the VHP-Male model is based exclusively on medical data collected as part of the US Library of Medicine's Visible Human Project [1, 7]. Conducted during the mid-1990s to late 1990s, this effort is a collection of extremely detailed and anatomically accurate data obtained from one male and one female cadaver. The data includes magnetic resonance imagery (MRI) and computed tomography (CT) imagery together with high-definition photographs of cross-sectional cryosections. This data is provided to the greater public free of charge, enabling a staggering number of applications, from medical research to artistic endeavours.

More specifically, the male data, released in 1994, includes axial MRI data collected at 4 mm intervals throughout the majority of the body, axial CT data collected at 1 mm intervals and anatomical cryosection images collected at 1 mm intervals to coincide with the CT data. These cryosection images are 2048 by 1216 pixels, with each pixel measuring 0.33 mm in size.

2.2 Mesh Construction

The VHP cryosection images were segmented using a custom MATLAB-based segmentation tool. Each cryosection image at a given height of the cadaver and oriented along the global Z axis was imported, and a user of this tool was able to surround a given structure with points denoting the X and Y axis limits of the structure. Once all images were processed in this manner, all X, Y and Z points were assembled such that they consisted of a point cloud describing the outer surface of the structure of interest. This point cloud was then meshed using triangular surface elements such that mesh became two-manifold.

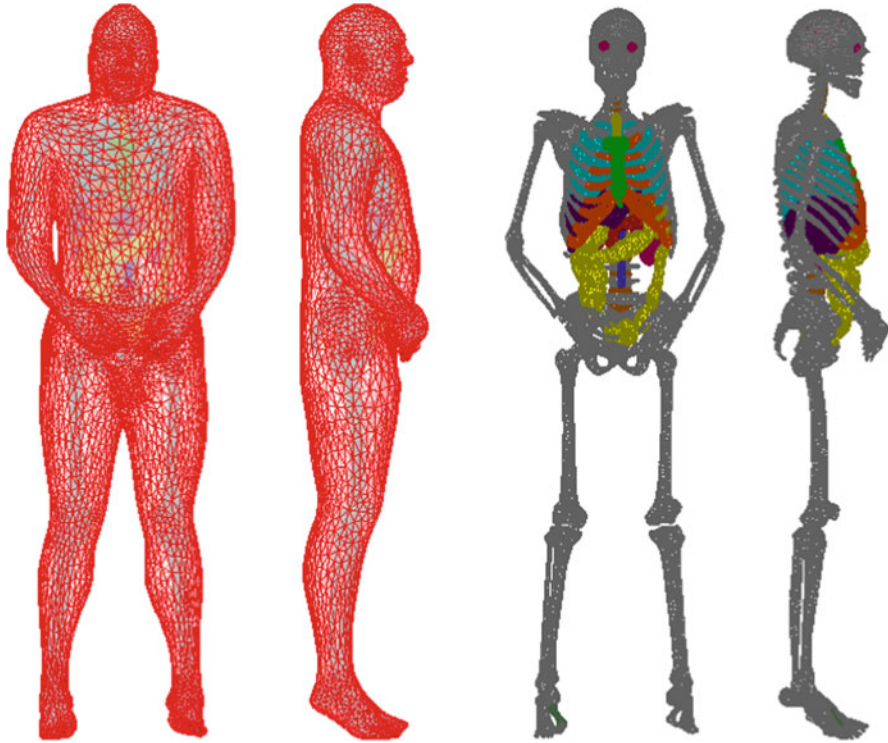


Fig. 1 The VHP-Male model. At left and mid-left: the full model including outer skin shell. At mid-right and right: the full model with the outer skin shell removed for better viewing of internal structures

Following segmentation and construction of each individual component, all components were assembled in a global reference frame and tested for intersections. All intersections were resolved using the mesh sculpting capabilities of Meshmixer. This tool is able to gradually move a triangle and its nearest neighbours along the triangle surface normal.

In certain instances, a smaller number of triangles were desired due to the need to balance simulation efficiency with model accuracy. In these cases, the quadric edge collapse decimation scheme [5] implemented in Meshlab was employed to reduce the number of triangles.

The results of these mesh manipulations are shown in Figs. 1, 2, 3 and 4. Each mesh component, the total number of triangles, mesh quality and the minimum mesh edge are given in Table 1.

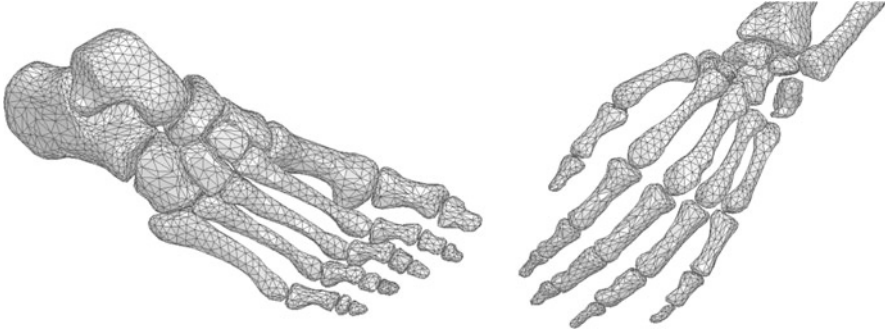


Fig. 2 Left – detailed views of the VHP-Male model foot and ankle; right – detailed views of the VHP-Male model hand and wrist

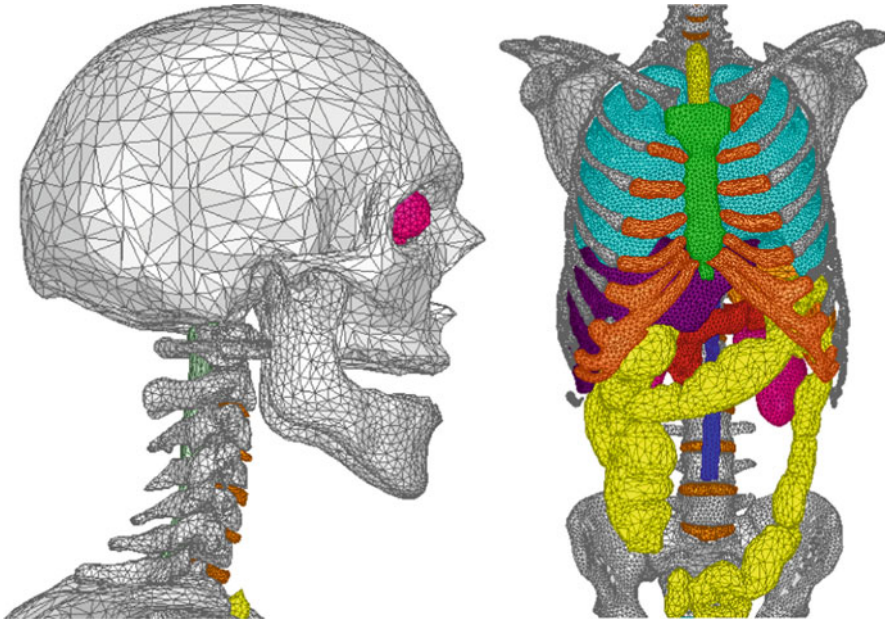


Fig. 3 Left – detailed view of the VHP-Male model skull and mandible; right – detailed views of the VHP-Male model internal organs and rib cage

2.3 *Simulation Setup*

Each component of the model was imported into the commercial FEM-based ANSYS Electromagnetics Suite 2019 R1 as an STL file and assigned dielectric and density material properties consistent with those published in the IT'IS Foundation [6]; this database has been widely accepted as the standard by the academic community. The excitation for this baseline simulation was a 300 MHz incident

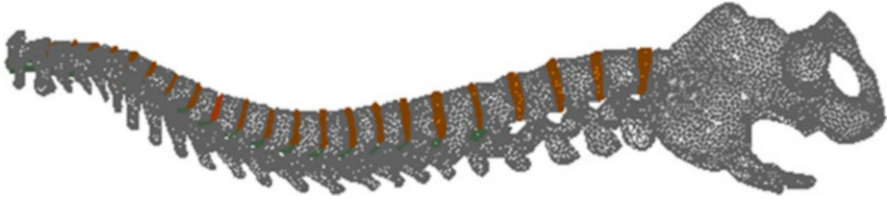


Fig. 4 Left – detailed views of the VHP-Male model spinal cord and vertebrae

plane wave with an intensity of 1 V/m originating approximately 35 mm in front of the model nose. The wave direction of propagation was toward the body, and the positive direction of the electric field was aligned with the positive vertical axis of the model.

Construction of the initial mesh was accomplished using the ‘Classic’ method, and mesh entity error checks were performed with the ‘Strict’ setting to ensure that no intersections or other mesh faults were present.

A solution setup with a target frequency of 300 MHz was applied and included adaptive mesh refinement. Following completion of the solution calculation, the volumetric mesh was refined by 30%. The resulting mesh statistics are presented in Table 2 along with simulation times and memory requirements. First-order basis functions were applied throughout. All calculations were performed by activating the HPC option and using 40 cores. The system hosting the software was running 64-bit Windows Server 2016 Standard with 64 AMD Opteron processors running at 2.66 GHz and a total of 256 GB of memory.

3 Results and Discussion

Following the initialization process described above, a triangular surface mesh composed of 313,750 elements was produced. This resulted in an initial volumetric mesh of 1,110,200 tetrahedra. Two adaptive mesh refinement steps were executed, documented in Table 2, generating a final mesh of 1,443,265 tetrahedra.

Plots of the magnitude of the electric field in the centres of the model sagittal and coronal planes are given in the top and bottom of Fig. 5, respectively. It is interesting to see the propagation of the surface wave along the skin shell in the sagittal plane. Also of note is the relatively uniform propagation of the wave within the body, shown in stark detail at the rear base of the neck; this is likely a consequence of the fact that the internal body volume was modelled with a single value of electrical permittivity and conductivity. When additional muscle structures are added, this is expected to greatly disrupt the path of the field, creating a much more inhomogeneous profile. Additional muscles will be added in the next model revision.

Table 1 Individual mesh names, number of triangles per mesh, triangle quality and minimum edge length

Mesh name	Triangles	Triangle quality	Min. edge length
'AortaLower'	1362	0.134330781	0.920544358
'AortaUpper'	652	0.222094966	1.260477698
'Bladder'	1640	0.068304298	0.812577699
'BrainWhiteMatter'	22,402	0.046567698	0.872950257
'CalcaneusLeft'	1344	0.114427155	1.452797748
'CalcaneusRight'	1412	0.097310098	1.564575094
'CapitateRight'	196	0.072770684	1.559374091
'CapitateLeft'	178	0.230362472	1.800466459
'Cerebellum'	2622	0.157891988	0.494216188
'ClavicleLeft'	1258	0.045264776	1.371140432
'ClavicleRight'	1238	0.078624045	1.213447698
'Coccyx'	346	0.06891789	0.908385343
'Colon'	7260	0.001621858	0.544420676
'CuboidLeft'	506	0.202039927	1.281321767
'CuboidRight'	500	0.175812595	1.436882414
'CuniformIntermediateLeft'	252	0.162846331	1.087986024
'CuniformIntermediateRight'	210	0.196727483	1.432081059
'CuniformLateralLeft'	314	0.066617761	1.440015526
'CuniformLateralRight'	282	0.244729955	1.658142044
'CuniformMedialLeft'	390	0.138902069	1.28087339
'CuniformMedialRight'	406	0.214556367	1.330687259
'DiscC03C04'	182	0.198568394	0.896118632
'DiscC04C05'	224	0.341427842	1.366489723
'DiscC05C06'	344	0.139070512	0.551801066
'DiscC06C07'	320	0.149239492	0.490609829
'DiscC07T01'	410	0.225282064	0.949094485
'DiscL01L02'	538	0.250568351	1.366702091
'DiscL02L03'	614	0.194281326	1.534183401
'DiscL03L04'	774	0.182906967	1.272352431
'DiscL04L05'	724	0.17660326	1.232707083
'DiscL05L06'	910	0.106356352	1.239995701
'DiscL06S00'	718	0.13029574	1.206016825
'DiscT01T02'	588	0.139201049	0.465434502
'DiscT02T03'	590	0.312950053	0.630624001
'DiscT03T04'	592	0.123513989	0.874712503
'DiscT04T05'	732	0.293476947	0.580976494
'DiscT05T06'	686	0.178928426	0.910670175
'DiscT06T07'	696	0.17695128	0.658382169
'DiscT07T08'	754	0.239607771	0.768537297
'DiscT08T09'	582	0.149629995	0.925819093
'DiscT09T10'	634	0.232195174	0.979317946
'DiscT10T11'	744	0.251148608	1.013260169

(continued)

Table 1 (continued)

Mesh name	Triangles	Triangle quality	Min. edge length
'DiscT11T12'	750	0.104616503	1.140370543
'DiscT12L01'	802	0.073026765	0.906750275
'Oesophagus'	2012	0.052368945	1.018606107
'FemurLeft'	5238	0.504688464	2.29075216
'FemurRight'	6128	0.549623054	2.480630149
'FibulaLeft'	2232	0.308788783	1.02925398
'FibulaRight'	2388	0.158261673	1.125755996
'GallBladder'	490	0.085184055	1.368812877
'HipLeft'	5772	0.170565242	0.466692974
'HipRight'	5596	0.066202543	0.577033756
'HumerusLeft'	3222	0.525440799	2.029104712
'HumerusRight'	2956	0.518585689	2.544932279
'KidneyLeft'	2264	0.103633477	0.475712171
'KidneyRight'	1922	0.185812015	0.568609335
'Lens_Left'	66	0.069840435	0.151185182
'Lens_Right'	150	0.120496855	0.307647016
'Liver'	10,920	0.029780084	0.517502817
'LunateLeft'	188	0.163375398	0.70472835
'LunateRight'	194	0.142373039	0.633063654
'LungLeft'	10,034	0.00168764	0.361124034
'LungRight'	10,094	0.06703563	0.396727705
'Mandible'	5000	0.097637404	0.261716653
'MetacarpalLeft1'	382	0.33160287	0.299037544
'MetacarpalLeft2'	426	0.298271901	1.3603719
'MetacarpalLeft3'	508	0.10321164	0.556610664
'MetacarpalLeft4'	308	0.085347552	0.972818976
'MetacarpalLeft5'	264	0.176798859	0.748657523
'MetacarpalRight1'	382	0.11581314	1.086429111
'MetacarpalRight2'	434	0.05808032	1.022409002
'MetacarpalRight3'	474	0.090823214	0.988240084
'MetacarpalRight4'	310	0.262561401	1.026288459
'MetacarpalRight5'	252	0.457876386	1.050913568
'MetatarsalLeft1'	652	0.120767953	0.517845995
'MetatarsalLeft2'	452	0.141255045	1.124870802
'MetatarsalLeft3'	462	0.172389284	0.574780219
'MetatarsalLeft4'	424	0.132385844	0.558378787
'MetatarsalLeft5'	444	0.249921383	0.900482375
'MetatarsalRight1'	652	0.119668442	0.706069735
'MetatarsalRight2'	446	0.214312152	0.710267704
'MetatarsalRight3'	414	0.195978651	0.874267734
'MetatarsalRight4'	414	0.24698425	1.14134027
'MetatarsalRight5'	438	0.153710476	0.807904513

(continued)

Table 1 (continued)

Mesh name	Triangles	Triangle quality	Min. edge length
'NavicularLeft'	460	0.206977803	0.99978752
'NavicularRight'	444	0.128297957	0.964590002
'Pancreas'	2102	0.203865066	0.745068684
'PatellaLeft'	530	0.267932417	1.078763998
'PatellaRight'	532	0.335488394	1.427379689
'PhalangeDistalFootLeft1'	168	0.235004346	1.571741849
'PhalangeDistalFootLeft2'	92	0.268369191	0.831078757
'PhalangeDistalFootLeft3'	102	0.483981354	1.352923578
'PhalangeDistalFootLeft4'	96	0.464114316	1.052147256
'PhalangeDistalFootLeft5'	82	0.202013722	1.015984979
'PhalangeDistalFootRight1'	180	0.096299624	1.353143922
'PhalangeDistalFootRight2'	116	0.302680933	1.125514542
'PhalangeDistalFootRight3'	70	0.343021658	1.204871773
'PhalangeDistalFootRight4'	170	0.31481353	0.721639691
'PhalangeDistalFootRight5'	72	0.469888115	1.122329106
'PhalangeDistalHandLeft1'	178	0.268247206	1.359285138
'PhalangeDistalHandLeft2'	130	0.09784967	1.292786241
'PhalangeDistalHandLeft3'	132	0.157418063	1.098169903
'PhalangeDistalHandLeft4'	168	0.250218437	0.879250144
'PhalangeDistalHandLeft5'	100	0.294543741	1.062110587
'PhalangeDistalHandRight1'	188	0.154548236	1.155781252
'PhalangeDistalHandRight2'	174	0.082593765	0.749666824
'PhalangeDistalHandRight3'	158	0.144122875	1.006352412
'PhalangeDistalHandRight4'	120	0.051107021	1.366663165
'PhalangeDistalHandRight5'	128	0.204927838	0.672745153
'PhalangeIntermediateFootLeft2'	126	0.19671167	1.202773185
'PhalangeIntermediateFootLeft3'	102	0.292676446	1.179335756
'PhalangeIntermediateFootLeft4'	94	0.28205998	1.319829723
'PhalangeIntermediateFootLeft5'	128	0.465058544	0.712763519
'PhalangeIntermediateFootRight2'	122	0.425226618	1.229020296
'PhalangeIntermediateFootRight3'	154	0.234524916	1.159242431
'PhalangeIntermediateFootRight4'	72	0.212530112	1.190552138
'PhalangeIntermediateFootRight5'	74	0.222513152	1.097581791
'PhalangeIntermediateHandLeft2'	162	0.056994087	1.403116851
'PhalangeIntermediateHandLeft3'	244	0.090014565	1.144600211
'PhalangeIntermediateHandLeft4'	206	0.234766368	1.32785976
'PhalangeIntermediateHandLeft5'	156	0.159150685	1.287847653
'PhalangeIntermediateHandRight2'	188	0.245103352	1.179043396
'PhalangeIntermediateHandRight3'	268	0.111289314	1.036930209
'PhalangeIntermediateHandRight4'	218	0.026740507	0.927233326
'PhalangeIntermediateHandRight5'	184	0.103672908	1.272412621
'PhalangeProximalFootLeft1'	316	0.166227126	1.328956537

(continued)

Table 1 (continued)

Mesh name	Triangles	Triangle quality	Min. edge length
'PhalangeProximalFootLeft2'	210	0.191881761	1.421797168
'PhalangeProximalFootLeft3'	204	0.183090128	1.153649369
'PhalangeProximalFootLeft4'	166	0.16043228	1.435088718
'PhalangeProximalFootLeft5'	184	0.280139704	1.35571498
'PhalangeProximalFootRight1'	358	0.17528083	1.13358412
'PhalangeProximalFootRight2'	172	0.109310553	1.493342579
'PhalangeProximalFootRight3'	184	0.176204429	1.46978673
'PhalangeProximalFootRight4'	198	0.190545609	1.103740172
'PhalangeProximalFootRight5'	208	0.110182825	1.080280334
'PhalangeProximalHandLeft1'	210	0.098640872	1.447996794
'PhalangeProximalHandLeft2'	272	0.199974342	1.451075053
'PhalangeProximalHandLeft3'	312	0.121724447	1.586284823
'PhalangeProximalHandLeft4'	294	0.165683911	1.321214895
'PhalangeProximalHandLeft5'	222	0.253583311	1.355428709
'PhalangeProximalHandRight1'	212	0.222933219	1.650829938
'PhalangeProximalHandRight2'	272	0.177067742	1.478012517
'PhalangeProximalHandRight3'	360	0.121158269	1.168497
'PhalangeProximalHandRight4'	354	0.223749458	1.367527605
'PhalangeProximalHandRight5'	222	0.239075957	1.495746015
'PisiformLeft'	78	0.314852312	2.176323052
'PisiformRight'	86	0.284437859	1.511736134
'RadiusLeft'	1624	0.07812625	1.580472228
'RadiusRight'	1652	0.005233192	1.677186851
'RibLeft01'	588	0.060906359	1.059913319
'RibLeft01Cartilage'	404	0.109004079	1.054736417
'RibLeft02'	1042	0.09086824	0.932675145
'RibLeft02_Cartilage'	176	0.045449305	2.127295566
'RibLeft03'	1128	0.113561227	0.99423192
'RibLeft03_Cartilage'	260	0.026268431	1.645999605
'RibLeft04'	1302	0.084563472	0.992262712
'RibLeft04_Cartilage'	308	0.023780717	1.636533296
'RibLeft05'	1274	0.119127187	0.984158072
'RibLeft05_Cartilage'	386	0.111179556	1.617471712
'RibLeft06'	5008	0.03157469	0.243544913
'RibLeft06_09Cartilage'	1792	0.100098473	0.591946184
'RibLeft07'	2510	0.036709266	0.61452184
'RibLeft08'	2496	0.110317453	0.545243404
'RibLeft09'	5026	0.033871361	0.259944831
'RibLeft10'	5018	0.001194147	0.201178192
'RibLeft10Cartilage'	220	0.239513906	1.157833434
'RibLeft11'	1148	0.108452456	1.019565359
'RibLeft12'	530	0.1788179	0.907150243

(continued)

Table 1 (continued)

Mesh name	Triangles	Triangle quality	Min. edge length
'RibRight01'	600	0.087526113	1.204959997
'RibRight02'	1148	0.10756514	0.511703818
'RibRight02_Cartilage'	212	0.225162533	1.718796537
'RibRight03'	1236	0.099341824	0.919209026
'RibRight03_Cartilage'	340	0.040870397	1.163855878
'RibRight04'	1224	0.137964912	1.049346668
'RibRight04_Cartilage'	340	0.123182198	1.852387423
'RibRight05'	1250	0.079547932	1.155101801
'RibRight05_Cartilage'	366	0.121168084	1.80995292
'RibRight06'	1330	0.176484463	1.038825487
'RibRight06_09Cartilage'	1902	0.102953268	1.104599593
'RibRight07'	2290	0.02321827	0.436906477
'RibRight08'	2470	0.035852455	0.697197243
'RibRight09'	2488	0.007762291	0.869718583
'RibRight10'	410	0.187648969	0.881692954
'RibRight12'	872	0.12421912	0.833364362
'Sacrum'	7146	0.005022698	0.121273699
'ScaphoidLeft'	276	0.161552246	1.259282022
'ScaphoidRight'	234	0.126420481	0.919981639
'ScapulaLeft'	2118	0.002681555	0.905832545
'ScapulaRight'	2064	0.003680874	0.996482213
'Skin'	13,246	0.000609802	0.198862826
'Skull'	14,766	0.001814466	0.154270982
'SpineC1'	2460	0.00481742	0.248172617
'SpineC2'	1190	0.08315216	0.781631363
'SpineC3'	1518	0.042719709	0.252149084
'SpineC4'	1794	0.002418403	0.038447994
'SpineC5'	1704	0.019635973	0.021795812
'SpineC6'	1702	0.007202928	0.020272316
'SpineC7'	1532	0.063678597	0.188076348
'SpineL1'	2790	0.105967936	0.545063665
'SpineL2'	2214	0.169298277	0.590225123
'SpineL3'	2014	0.022869325	0.758650269
'SpineL4'	2072	0.010869297	0.55886578
'SpineL5'	1906	0.143658437	1.191150819
'SpineT1'	1356	0.033942145	0.248312562
'SpineT10'	1598	0.071890258	0.599400251
'SpineT11'	1746	0.099742236	0.411570228
'SpineT12'	1770	0.204306553	0.734127338
'SpineT2'	1546	0.004042741	0.992247621
'SpineT3'	1370	0.11645742	0.356404699
'SpineT4'	1382	0.076971261	0.159364139

(continued)

Table 1 (continued)

Mesh name	Triangles	Triangle quality	Min. edge length
‘SpineT5’	1482	0.136731374	0.637760074
‘SpineT6’	1298	0.098502586	0.573448349
‘SpineT7’	1312	0.146509781	1.096860449
‘SpineT8’	2152	0.003031485	0.395329192
‘SpineT9’	1734	0.016899747	0.416672514
‘Spleen’	952	0.128410792	2.317553484
‘Sternum’	2336	0.017746966	0.595070383
‘TalusLeft’	914	0.522314047	1.397671978
‘TalusRight’	848	0.16043732	1.072112228
‘TibiaLeft’	4544	0.534577008	1.721629222
‘TibiaRight’	4296	0.59556915	2.341040932
‘TrapeziumLeft’	178	0.199925044	0.525153998
‘TrapeziumRight’	150	0.341799266	1.094954994
‘TrapezoidLeft’	148	0.067468983	0.507043705
‘TrapezoidRight’	128	0.130458037	0.663360569
‘TriquetralLeft’	182	0.069901248	0.329812317
‘TriquetralRight’	134	0.246326993	0.986282248
‘UlnaLeft’	1950	0.32301674	1.023958874
‘UlnaRight’	1998	0.137709703	0.985571845
‘VitreousHumor_Left’	312	0.416736477	0.50974078
‘VitreousHumor_Right’	268	0.266409301	1.142471306

Table 2 Individual mesh names, number of triangles per mesh, triangle quality and minimum edge length

Adaptive pass	Number of tetrahedra	Solver time (HH:MM:SS)	Memory (GB)
1	1,110,200	01:00:13	109
2	1,443,265	01:56:40	177

4 Conclusions

The work describes the construction and baseline use of the Visible Human Project (VHP)-Male computational phantom, a CAD-compatible model based on publicly available data. This model has been constructed such that it may be employed by all of the most common CEM simulation techniques in use today and easily modified to optimally fit a given application. A baseline simulation using the commercial FEM-based ANSYS Electromagnetics Suite 2019 was conducted, and the results of this simulation were presented.

Future additions to the model include major muscle groups and selected large nerves. In addition, further detail in the circulatory system will likely be required to address several simulation applications.

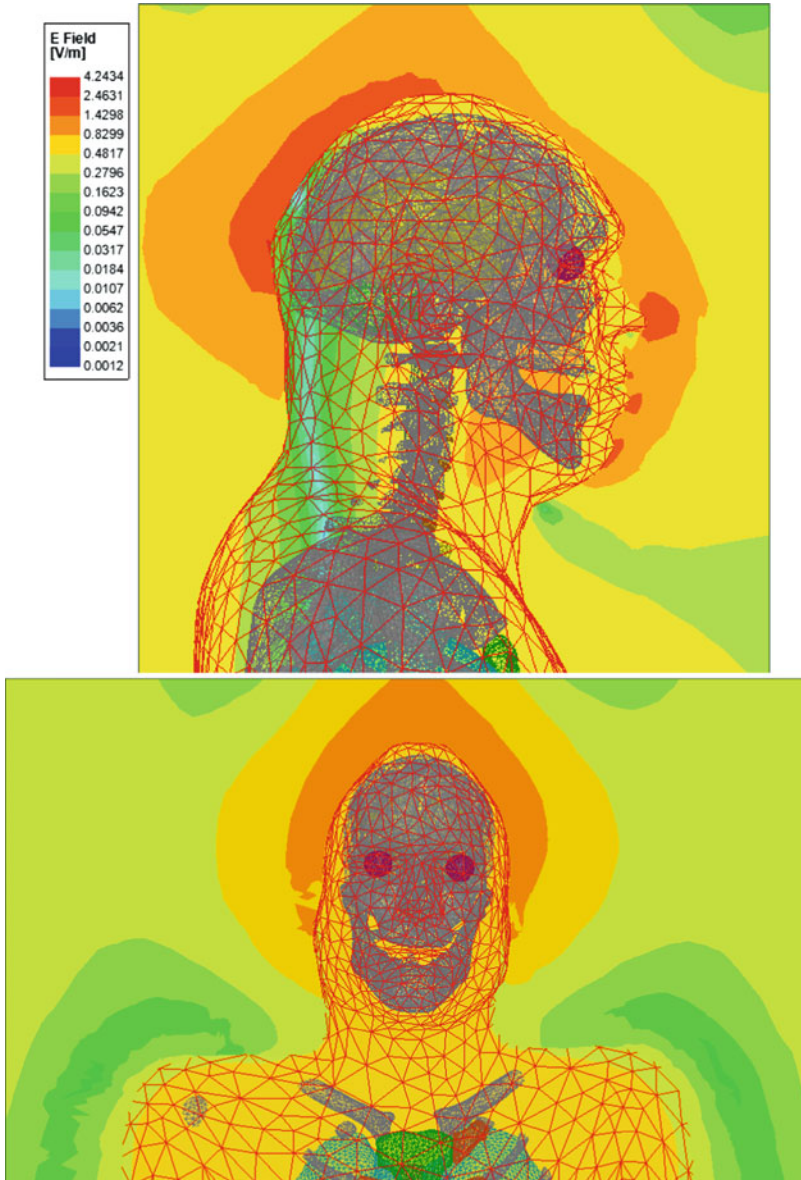


Fig. 5 Top – electric field magnitude at centre of sagittal plane; bottom – electric field magnitude at centre of coronal plane

As with the VHP-Female model, additional layers characterizing variations in skin and fat thicknesses will be included to explore the impact of body mass index on SAR. Refinements of the inner and outer ear structures are also envisioned. Inclusion of sinus cavities will also be critical to enable the highest level of accuracy possible.

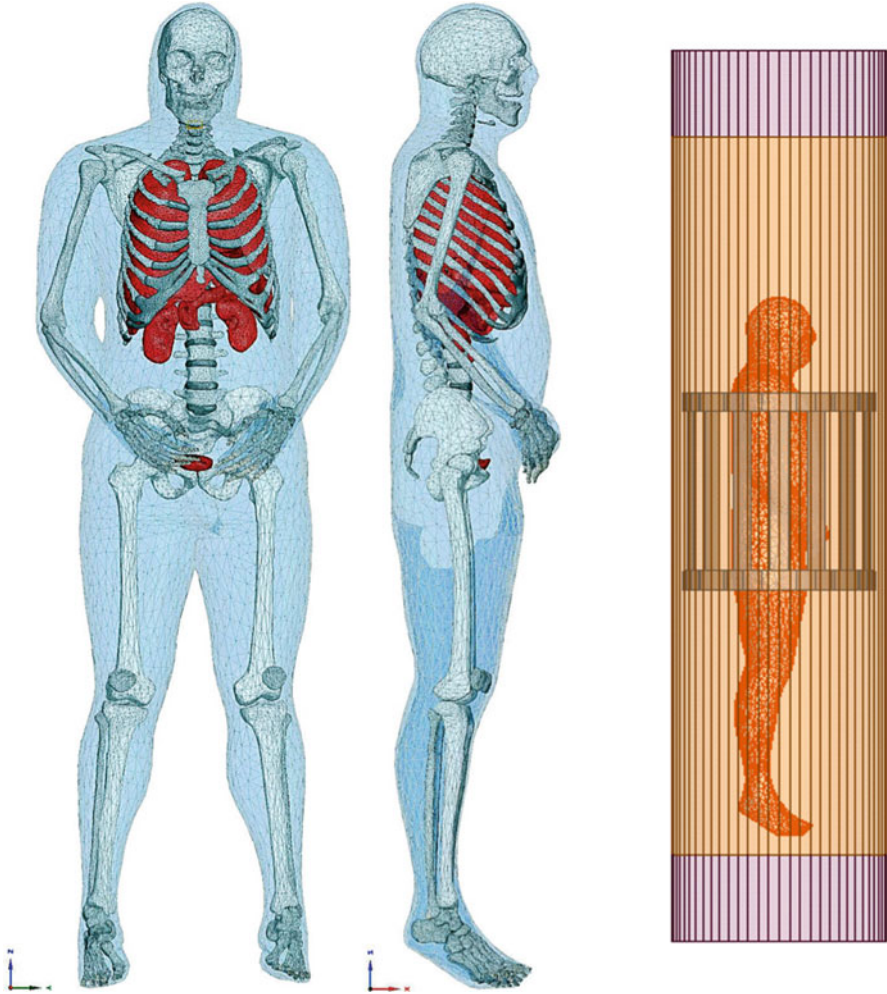


Fig. 6 The VHP-Male model oriented in a simulation of an MRI coil

Figure 6 provides one possible use of this new model: simulation of a loaded MRI coil. The VHP-Female model was used very successfully to characterize numerous MRI coil designs. There is no reason to believe this new male model would not also be highly suitable for this purpose.

Acknowledgements The author would like to thank Dr. Ali Yilmaz, Dr. Jackson Massey and the Computational Electromagnetics Group at the University of Texas at Austin for their exceptional work on the AustinMan and AustinWoman voxel models [11]. The AustinMan model in particular represented the standard against which the VHP-Male model was measured.

References

1. Ackerman, M. J. (1998, March). The visible human project. *Proceedings of the IEEE* (vol. 86, pp. 504–511).
2. Barbi, M., Garcia-Pardo, C., Cardona, N., Nevarez, N., Pons, V., & Frasson, M. (2018). Impact of receivers location on the accuracy of capsule endoscope localization. *2018 IEEE 29th annual international symposium on Personal, Indoor and Mobile Radio Communications (PIMRC)*, Bologna, (pp. 340–344). <https://doi.org/10.1109/PIMRC.2018.8580862>.
3. Chen, L. et al.. (2018, July). Radiofrequency propagation close to the human ear and accurate ear canal models. *40th Annual International Conference of the IEEE Engineering in Medicine and Biology Society (EMBC 2018)*, Honolulu, HI (pp.17–21).
4. Garcia-Pardo, C. et al.. (2018, June). Ultrawideband technology for medical in-body sensor networks: An overview of the human body as a propagation medium, phantoms, and approaches for propagation analysis. *IEEE Antennas and Propagation Magazine* 60(3): 19–33. <https://doi.org/10.1109/MAP.2018.2818458>.
5. Garland, M., & Heckbert, P. S. (1997). Surface simplification using quadric error metrics. *SIGGRAPH '97 Proceedings of the 24th Annual Conference on Computer Graphics and Interactive Techniques* (pp. 209–216). New York.
6. Hasgall, P. A., Di Gennaro, F., Baumgartner, C., Neufeld, E., Lloyd, B., Gosselin, M. C., Payne, D., Klingensböck, A., & Kuster, N. (2018, May 15). *IT'IS Database for thermal and electromagnetic parameters of biological tissues*. Version 4.0. <https://doi.org/10.13099/VIP21000-04-0>. [it is.swiss/database](http://www.itis.swiss/database).
7. U.S. National Library of Medicine. The Visible Human Project® Online: http://www.nlm.nih.gov/research/visible/visible_human.html
8. Lemdiasov, R., & Venkatasubramanian, A. (2017). Transmit coil design for Wireless Power Transfer for medical implants. *2017 39th Annual International Conference of the IEEE Engineering in Medicine and Biology Society (EMBC)*, Seogwipo (pp. 2158–2161). <https://doi.org/10.1109/EMBC.2017.8037282>.
9. Makarov, S. N., Noetscher, G. M., Yanamadala, J., Piazza, M. W., Louie, S., Prokop, A., Nazarian, A., & Nummenmaa, A. (2017). Virtual human models for electromagnetic studies and their applications. *IEEE Reviews in Biomedical Engineering*, 10, 95–121. <https://doi.org/10.1109/RBME.2017.2722420>.
10. Makarov, S. N., Noetscher, G. M., Raij, T., & Nummenmaa, A. (2018). A quasi-static boundary element approach with fast multipole acceleration for high-resolution bioelectromagnetic models. *IEEE Transactions on Biomedical Engineering*, 65(12), 2675–2683. <https://doi.org/10.1109/TBME.2018.2813261>.
11. Massey, J. W., & Yilmaz, A. E. (2016, Aug). AustinMan and AustinWoman: High-fidelity, anatomical voxel models developed from the VHP color images. In *Proceedings of 38th Annual International Conference of the IEEE Engineering in Medicine and Biology Society (IEEE EMBC)*. Orlando.
12. Nikolayev, D. (2018). Modeling and Characterization of in-Body Antennas,” *2018 IEEE 17th international conference on Mathematical Methods in Electromagnetic Theory (MMET)*, Kiev (pp. 42–46). <https://doi.org/10.1109/MMET.2018.8460279>.
13. Nikolayev, D., Zhadobov, M., Karban, P., & Sauleau, R. (2017, December). Conformal antennas for miniature in-body devices: The quest to improve radiation performance. *URSI Radio Science Bulletin 2017*(363):52–64. <https://doi.org/10.23919/URSIRSB.2017.8409427>
14. Nikolayev, D., Zhadobov, M., Le Coq, L., Karban, P., & Sauleau, R.. (2017, November). Robust Ultraminiature capsule antenna for ingestible and implantable applications. *IEEE Transactions on Antennas and Propagation* 65(11): 6107–6119. <https://doi.org/10.1109/TAP.2017.2755764>.
15. Noetscher, G. et al. (2016, August). Computational Human Model VHP-FEMALE Derived from Datasets of the National Library of Medicine,” *38th Annual International Conference of the IEEE Engineering in Medicine and Biology Society (EMBC 2016)*, Orlando. (pp. 16–20.)

16. Perez-Simbor, S., Andreu, C., Garcia-Pardo, C, Frasson, M., & Cardona, N. UWB Path Loss Models for Ingestible Devices. *IEEE Transactions on Antennas and Propagation*. <https://doi.org/10.1109/TAP.2019.2891717>
17. Venkatasubramanian, A., & Gifford, B. (2016). Modeling and design of antennas for implantable telemetry applications. 2016 38th Annual International Conference of the IEEE Engineering in Medicine and Biology Society (EMBC), Orlando (pp. 6469–6472). <https://doi.org/10.1109/EMBC.2016.7592210>.

Open Access This chapter is licensed under the terms of the Creative Commons Attribution 4.0 International License (<http://creativecommons.org/licenses/by/4.0/>), which permits use, sharing, adaptation, distribution and reproduction in any medium or format, as long as you give appropriate credit to the original author(s) and the source, provide a link to the Creative Commons license and indicate if changes were made.

The images or other third party material in this chapter are included in the chapter’s Creative Commons license, unless indicated otherwise in a credit line to the material. If material is not included in the chapter’s Creative Commons license and your intended use is not permitted by statutory regulation or exceeds the permitted use, you will need to obtain permission directly from the copyright holder.

